

Research Paper

Mechanisms facilitating the uptake of carboxyl–polythene glycol-functionalized gold nanoparticles into multicellular spheroids

Seth-Frerich Fobian¹, Melissa Petzer¹, Melissa Vetten², Vanessa Steenkamp¹,
Mary Gulumian^{2,3,4} and Werner Cordier^{1,*}

¹Department of Pharmacology, Faculty of Health Sciences, University of Pretoria, Pretoria, South Africa

²Toxicology Section, National Institute for Occupational Health, National Health Laboratory Service, Johannesburg, South Africa

³Molecular Medicine and Haematology, School of Pathology, University of Witwatersrand, Johannesburg, South Africa

⁴Water Research Group, Unit for Environmental Sciences and Management, North-West University, Potchefstroom, South Africa

*Correspondence: Werner Cordier, Department of Pharmacology, Faculty of Health Sciences, University of Pretoria, Private Bag X323, Arcadia 0007, South Africa. Email: werner.cordier@up.ac.za

Abstract

Objectives Nanomedicines represent theragnostic alternatives to traditional candidate drugs, with increased targeting and delivery potential due to their size and functional tailorability. Biological activity typically relies on nanomaterials permeating into the intracellular environment, necessitating characterization of uptake and intracellular trafficking pathways. Spheroids' three-dimensional architecture and heterogenous cellular distribution offer an in-vivo-representative platform to assess the biological activity of nanoparticles (NPs). This study aimed to develop an A549 alveolar carcinoma spheroid model as a NP uptake assessment platform for carboxyl–polythene glycol-functionalized gold NPs affording further biological characterization opportunities in nanomedicine.

Methods A549 spheroids were generated via the liquid overlay method, and their morphology and viability were assessed for 21 days. Cytotoxicity was assessed via lactate dehydrogenase release. NP uptake was elucidated using uptake pathway inhibition, combined with CytoViva hyperspectral imaging of sectioned spheroids to count internalized NPs.

Key findings Cytotoxicity was absent for all exposure groups. Clathrin-mediated endocytosis was the primary endocytic mechanism (33.5–54.8% of uptake), which may precede lysosomal degradation. Lysosomal membrane permeabilization appears to be a potential downstream application. Low penetration into spheroids (4.5 µm) suggests the failure of NPs to traverse cellular layers in the spheroid.

Conclusions Although poor uptake was observed, a multicellular spheroid model of A549 alveolar carcinoma cells was established, allowing for similar future uptake assessment of various NPs.

Keywords: clathrin-mediated endocytosis; CytoViva; gold nanoparticles; nanomedicine; spheroids; uptake

Introduction

Widespread investigation into nanomedicines (the use of nanomaterials in diverse medical applications) has increased in recent years, with particular interest in their targeting capabilities and relatively low cytotoxicity, stemming from the size and functional tailorability thereof.^[1] Nanomedicines are of interest in diagnostics (visualization and bioimaging), immunology (vaccines, biodistribution and cytotoxicity) and therapeutics (drug/gene delivery, anti-angiogenesis and radiofrequency and photothermal therapy).^[2–5] Various types of nanoparticles (NPs) are used in medicine, including quantum dots, superparamagnetic iron oxide NPs, carbon nanotubes, silica NPs, liposomes, dendrimers, nanogels and gold nanoparticles (AuNPs).^[6] Gold NPs' clinical applications span diagnostics, therapeutics and drug delivery, thereby making them appealing and versatile nanomedical candidates.

Inherent anticancer activity has also been observed in AuNPs, by way of reactive oxygen species (ROS)-induction, anti-angiogenesis and lysosomal membrane permeabilization (LMP).^[5, 7–12] The latter is a powerful mechanism of cytotoxicity, causing leakage of degradative lysosomal enzymes into the cytoplasm and subsequent autophagy.^[8]

Cellular uptake pathways (Figure 1) mediate most of a cell's responses to external stimuli; thus, hindered biological activity may be observed should an agent lack intracellular access.^[13, 14] Most macromolecules and particles gain entry to the intracellular environment via endocytosis.^[15] The uptake mechanisms and intracellular destinations of many NP types have not yet been described.^[15] NP uptake has been associated primarily with clathrin-mediated endocytosis (CME); however, other pathways, including caveolae-mediated endocytosis (CvME) and passive diffusion, may contribute.^[13, 16, 17]

Received: September 28, 2021. Editorial Acceptance: February 23, 2022

© The Author(s) 2022. Published by Oxford University Press on behalf of the Royal Pharmaceutical Society.

This is an Open Access article distributed under the terms of the Creative Commons Attribution-NonCommercial-NoDerivs licence (<https://creativecommons.org/licenses/by-nc-nd/4.0/>), which permits non-commercial reproduction and distribution of the work, in any medium, provided the original work is not altered or transformed in any way, and that the work is properly cited. For commercial re-use, please contact journals.permissions@oup.com

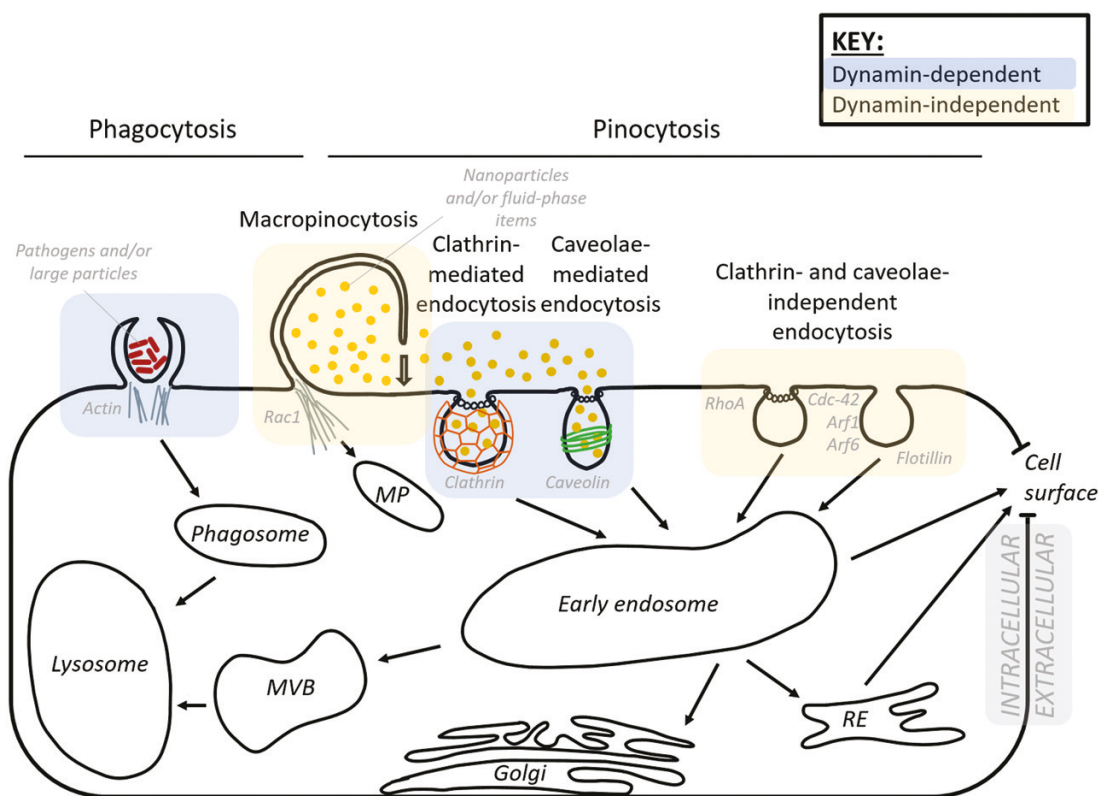


Figure 1 The major endocytic pathways of a hypothetical cell and intracellular trafficking mechanisms, differing based on size, shape, charge and phase of the external particles, as well as proteins involved.^[13, 15] Original graphic designed by the lead author. Abbreviations: Arf1/6, adenosine diphosphate ribosylation factor 1/6; Cdc-42, cell division control protein 42 homolog; MP, macropinosome; MVB, multivesicular body; Rac1, ras-related C3 botulinum toxin substrate 1; RE, recycling endosome; RhoA, ras homolog gene family member A.

An understanding of uptake pathways and the way they interact is crucial in demystifying intracellular targeting and therapeutic potentials of candidate drugs or drug-delivery agents – in this case, AuNPs.^[8, 18, 19] It is essential that such investigations occur in a biological setting representative of what may occur *in vivo*, which is generally not the case with traditional cell culture models.^[20]

Multicellular tumour spheroids are widely considered to be capable of bridging the gap between *in-vitro* and *in-vivo* systems by offering a simple, reproducible and more representative model, thus more appropriately simulating the cellular complexity of the tumour microenvironment.^[20–22] The predictive capability of these *in-vitro* systems is increased due to the superiority of three-dimensional (3D) culturing over two-dimensional (2D) models to establish cell–cell and cell–matrix interactions, metabolic gradients, cell differentiation, gene regulation and cell cycle control.^[23–26] This is largely due to the deposition of extracellular matrix (ECM), which occurs upon aggregation of adherent cells with one another, resulting in the formation of compacted spheroids.^[27, 28] The ECM, comprising collagen, elastin, fibronectin, laminin and glycoproteins, opposes the unrestrained proliferation of monolayer cultures.^[29, 30] These factors provide mechanical structure to tissues; facilitate adhesion and homeostasis; and regulate cellular migration, proliferation and differentiation.^[31, 32] In this study, a drug discovery and toxicity testing platform was established using A549 alveolar carcinoma spheroids, with the goal of elucidating the uptake mechanisms used by this cell type for the pilot agent in this study: 14 nm carboxyl–polythene glycol-functionalized gold nanoparticles (PCOOH-AuNPs).

The A549 cell line was selected due to previous pulmonary cell studies on the PCOOH-AuNPs, as well as its relevance in pulmonary toxicity and anticancer studies.^[16, 33–36] The above model was used to assess the cells' primary uptake mechanisms used for the PCOOH-AuNPs and the intracellular destinations thereof. The implications of uptake mechanism selection are also discussed and contextualized for nanomedical applications. This study provided a two-pronged approach to address the global oncological shortfall of severe drug toxicity, primarily arising out of a lack of specificity. It includes investigation of effective drug-delivery mechanisms, using a newly characterized *in-vivo*-representative cellular platform for evaluation, thus providing a platform for investigation of similar mechanisms using other NPs and cell lines.

Materials and Methods

Materials

A549 alveolar carcinoma cells (CCL-185) were procured from the American Type Culture Collection (ATCC; Manassas, USA). Low gelling-temperature agarose, dimethyl sulfoxide (DMSO), heat-inactivated fetal calf serum (FCS), chlorpromazine, Dynasore, 5-(*N*-ethyl-*N*-isopropyl) amiloride (EIPA), genistein, penicillin/streptomycin, sodium azide and the fluorescent dyes, propidium iodide (PI) and fluorescein diacetate (FDA) were all procured from Merck (Darmstadt, Germany). Distilled water (dH₂O) was obtained from an ELGA PURELAB Chorus water purification system. The PCOOH-AuNPs were obtained from

Mintek (Randburg, South Africa). Fluorescent treponemal antibody (FTA) hemagglutination buffer [phosphate-buffered saline (PBS)] was procured from Becton, Dickinson and Company (Sparks, USA). The CytoTox-ONE homogeneous membrane integrity assay (lactate dehydrogenase [LDH]) kit was procured from Promega (Madison, USA). Gibco Dulbecco's modified eagle medium (DMEM) with phenol red and TrypLe express enzyme (phenol red free) were procured from ThermoFisher (Johannesburg, South Africa). Tissue-Tek O.C.T compound was procured from Sakura Finetek (Torrance, USA).

Ethical approval

This study, and the entirety of the experimentation referred to herein, including the use of the commercially available A549 cell line, was approved by the Research Ethics Committee of the University of Pretoria's Faculty of Health Sciences (REC #540/2019).

Synthesis and characterization of PCOOH-AuNPs

The manufacturing and functionalization of PCOOH-AuNPs were carried out as previously described.^[16,36] Briefly, aqueous solutions of sodium citrate and tetrachloroaurate were combined and boiled under reflux for 15 min. This solution was cooled overnight at room temperature (RT) under constant stirring and then filtered for sterility using a 0.25- μm syringe filter. This solution was functionalized by saturation with carboxylated polythene glycol (PEG-COOH) chains (Figure 2). These PCOOH-AuNPs have a molecular weight of 526.73 g/mol and possess a COOH group conjugated to a polythene (PEG) chain.^[16]

Assessment of NP interference

To assess potential chemical and physical interference, PCOOH-AuNPs were diluted in dH_2O or DMEM to 6.25×10^{11} NPs/ml to determine characteristics in different solutions. An aliquot of 100 μl PCOOH-AuNP suspension was measured using a Synergy II microplate reader (Biotek Instruments, Inc., Winooski, USA) both spectrophotometrically (200–800 nm) and fluorometrically (excitation/emission wavelengths; 485/590 nm). Additionally, possible interferences with the LDH assay substrate (resazurin) and fluorescent product (resorufin) were measured by incubating equal volumes (100 μl) of the substrate or product in the presence and absence of PCOOH-AuNPs, before measuring fluorescent activity.

Maintenance of the A549 alveolar carcinoma cell line

The A549 alveolar carcinoma cell line was cultured in 75- cm^2 cell culture flasks in DMEM supplemented with 10% FCS and 1% penicillin/streptomycin at 37°C in a humidified atmosphere of 5% CO_2 . At 80% confluence, the medium was decanted, and cells were washed with PBS. Cells were chemically detached using TrypLE express enzyme, centrifuged (200g for 5 min) in a 10% FCS-supplemented medium. The pellet was resuspended in 1 ml 10% FCS-supplemented medium and counted using the trypan blue exclusion assay (0.1% in PBS) and a haemocytometer.

Seeding and spheroid formation

The liquid overlay technique was employed for a spheroid generation.^[37] To create a low-attachment surface, 75 μl of 1.6% low gelling-temperature agarose was pipetted into clear, flat-bottom, 96-well plates, swirled to induce concavity, and allowed to solidify by cooling. The agarose solution was prepared by first creating a 4% (w/v) agarose solution in PBS, then diluting it to 1.6% using FCS-free DMEM. Edge wells received 200 μl sterile PBS to reduce evaporation. Cell suspension (100 μl , 7.5×10^4 cells/well) was seeded onto the agarose bed. Spheroids were kept in culture for a maximum of 21 days. Experiments requiring higher throughput made use of 9×9 3D Petri Dishes (Microtissues, Inc., Sharon, USA) for spheroid formation, yielding identical spheroids. The same agarose as above was used to form a mould yielding 81 spheroids, into which 190 μl cell suspension (7.5×10^4 cells/spheroid) was added. In all cases, cells were incubated for 72 h to allow for spheroid formation, with the medium being replenished every 3 days.

Spheroid growth and viability

Spheroid growth and viability were assessed on Days 4, 7, 10, 14, 18 and 21. Morphology was evaluated using phase-contrast microscopy [Zeiss Axiovert 200M inverted microscope (Carl Zeiss, Inc., Oberkochen, Germany)] and ImageJ to determine the circularity index and diameter.^[38,39] The spheroid's circularity index, indicating the degree of circularity on a scale from 0 (elongated polygon) to 1.0 (perfect circle), was calculated using the formula: $\text{Circularity} = 4\pi \left(\frac{\text{area}}{\text{perimeter}^2} \right)$.^[40]

Live/dead staining was used to confirm zones of viability and cell death within spheroids.^[29] Viable, metabolically active regions convert non-fluorescent FDA to the fluorescent

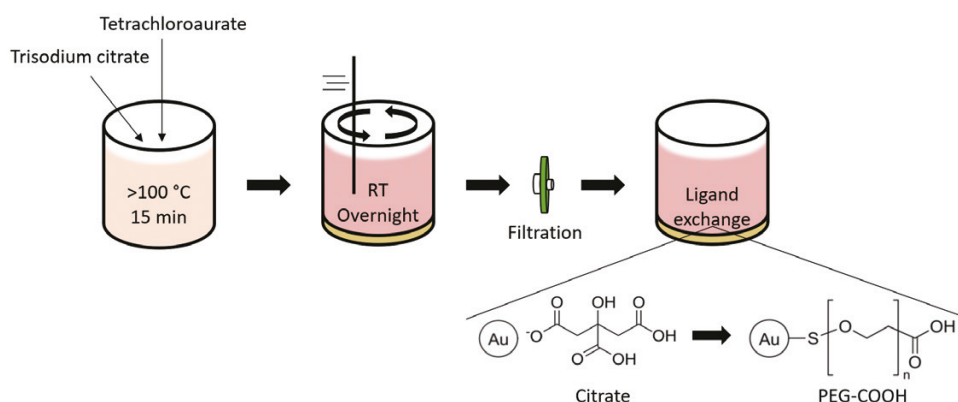


Figure 2 Simplified schematic of PCOOH-AuNP synthesis.

fluorescein,^[41] while PI intercalates with the nucleic acids of membrane-compromised cells, thus suggesting cell death.^[38,39] Spheroids were harvested and washed thrice with PBS. In a dark room, 1 ml FDA/PI (5 and 4 µg/ml, respectively) staining solution was added to each well. Spheroids were washed again with PBS, then immediately imaged using a Zeiss Axiovert 200M inverted microscope with filter sets for Texas red (for PI fluorescence) and fluorescein isothiocyanate (for FDA fluorescence). Images were processed and combined using ImageJ.

The release of LDH from lysed cells was quantified since it proportionally reflects cell growth.^[42] Spheroids found to have consistent size and form were selected for experimentation. Spheroids were transferred to opaque-walled 96-well plates, and the medium was replaced with 50 µl of medium containing 2% (v/v) CytoTox-ONE lysis solution. Cell-free blanks were included to account for background noise. Plates were incubated for 5 min at RT, after which 50 µl CytoTox-ONE reagent was added to each well. The plates were shaken for 1 min, incubated for 10 min at RT and the fluorescence intensity (FI) read (emission/excitation wavelengths of 485/590 nm, respectively). All values were blank-subtracted, averaged and expressed as a percentage of growth at Day 4, using the equation (*y* denoting number of days since Day 4):

$$\text{Growth (\% relative to Day4)} = \frac{\text{Average FI(Day } y)}{\text{Average FI(Day 4)}} \times 100.$$

Assessment of cytotoxicity in spheroids

The cytotoxicity of PCOOH-AuNPs and the uptake inhibitors was assessed using the LDH release assay. Cytotoxicity testing was performed on Day 7 spheroids. Medium was aspirated from spheroids and replaced with 50 µl DMEM alone (negative control) or supplemented with 0.4% (v/v) DMSO (vehicle control), 2% (v/v) CytoTox-ONE lysis solution (positive lysis control), 6.25 × 10¹¹ NPs/ml PCOOH-AuNP or pharmacological inhibitors (concentrations provided in Table 1). A blank consisting of 50 µl DMEM only was used to control for background noise. Spheroids were exposed for 2 and 24 h to PCOOH-AuNPs alone, and for 3 h to pharmacological inhibitors (a period exceeding that of literature-based time needed to inhibit uptake systems). The LDH release was compared with that of the negative control.

Elucidation of cellular uptake mechanism(s) used by spheroids for NP uptake

Incubation with pharmacological inhibitors and PCOOH-AuNPs for uptake inhibition assay

The uptake mechanism employed for PCOOH-AuNPs was determined using the adapted method of Vetten *et al.*, which involves pharmacological uptake inhibitors (Table 1) to selectively reduce the activity of specific uptake pathways (treatment regimens provided in Figure S1).^[16] Spheroids' medium

was replaced with 100 µl DMEM alone or supplemented with pharmacological inhibitors or 0.4% (v/v) DMSO (vehicle control) for 1 h at 37°C. Thereafter, 33 µl of PCOOH-AuNP stock suspension was added to each well to achieve a final concentration of 6.25 × 10¹¹ NPs/ml and incubated for a further 2 h at 37°C. An additional 24 h exposure timepoint was included for the uninhibited PCOOH-AuNP sample alone to assess longer-term uptake thereof.

Sectioning of spheroids for analysis

Before sectioning, the medium was aspirated and spheroids were transferred onto an aluminium grid. Single spheroids were then immersed in Tissue-Tek and frozen at -30°C. A Shandon Cryotome E (Thermo Scientific, Waltham, USA) was used to create 5 µm sections which were transferred directly to glass slides for storage and subsequent microscopy.

Hyperspectral imaging using CytoViva

Samples were viewed at ×60 magnification on the CytoViva hyperspectral imaging (HSI) system (CytoViva, Inc., Auburn, USA), integrated onto an Olympus BX43 microscope, available at the National Institute for Occupational Health. Dark field images were acquired using a Dageexcel X16 camera, and hyperspectral scans of the sectioned spheroids were captured using ENVI 4.8 software. The CytoViva system enables a label-free approach to intracellular NP detection with non-destructive sample preparation.^[50] HSI and spectral angle mapping (SAM) were used to assess intracellular uptake by counting PCOOH-AuNPs present intracellularly in a defined area. The particle filter feature was used to create a spectral library for the PCOOH-AuNPs, based on the spectra acquired from a scan of NPs within spheroid sections of the uninhibited uptake control, as detailed in the method by Roth *et al.*^[50] This approach allows for the subtraction of the negative control to remove the spectra of the cellular background. SAM was used to match the spectral library onto corresponding pixels in the hyperspectral scans of the PCOOH-AuNP-treated cells, thereby confirming particle presence. ImageJ was then used to obtain a count for PCOOH-AuNPs taken up by the spheroids within a region of interest of fixed area (*A*). Data obtained in this way were used as semi-quantitative measures of PCOOH-AuNP uptake in the absence or presence of pharmacological inhibitors. NP uptake was calculated as a percentage of the uninhibited control using the equation:

$$\begin{aligned} & \frac{NP}{A} (\% \text{ relative to uninhibited positive control}) \\ &= \frac{\text{Average } \frac{NP}{A} (\text{inhibited experiment})}{\text{Average } \frac{NP}{A} (\text{uninhibited positive control})} \times 100 \end{aligned}$$

Table 1 Inhibitory concentrations and targeting of pharmacological uptake inhibitors

Inhibitor	Mechanism of action (process inhibited) [reference]	Concentration [reference]
Sodium azide	ATPase inhibition (all active transport) ^[43]	10 mM ^[44]
Dynasore	Dynamin inhibition (dynamin-dependent pathways) ^[15]	80 µM ^[44,45]
EIPA	F-actin reorganization, pseudopodia retraction (macropinocytosis and phagocytosis) ^[46,47]	25 µM ^[46,48]
Genistein	Tyrosine kinase and dynamin inhibition, actin network disruption (CvME) ^[15,49]	200 µM ^[16]
Chlorpromazine	Rho GTPase inhibition (CME) ^[15,49]	14 µM ^[16]

Abbreviations: ATPase, adenosine triphosphatase; GTPase, guanosine triphosphatase.

Statistical analyses

Statistical analyses were carried out using Microsoft Excel and GraphPad Prism 5. All data were expressed as mean \pm standard error with at least three biological, and three technical, repeats. Statistical significance was set at P values < 0.05 . Comparisons to the negative controls were made using a Kruskal–Wallis test with *post hoc* Dunn's test.

Results

Gold NP characterization

The 14-nm PCOOH-AuNPs were provided at a stock concentration of 2.5×10^{12} NPs/ml (equivalent to 4.1 nM). Suspended in DMEM, the PCOOH-AuNPs possessed a ζ -potential (surface charge) of -13.7 mV as measured by the Zetasizer Nano ZS (Malvern) with a size variance of 2 nm (measured by transmission electron microscopy at Mintek). Ultraviolet–visible spectroscopy (UV-Vis) spectroscopy (Figure 3A) revealed spectral peaks at 520 and 560 nm when suspended in dH_2O and DMEM, respectively. Negligible autofluorescence was observed (Figure 3B) at excitation/emission wavelengths of 485/590 nm. Non-significant quenching of resorufin (5.26%) and conversion of resazurin (0.6%) were observed (Figure 3C and D).

Spheroid morphology and growth

Spheroids gradually increased in diameter over the first 10 days (Figure 4A). On Day 7, an average diameter and circularity index of 702.11 ± 10.77 and 0.80 ± 0.03 μm , respectively, were observed. Diameter continued to increase after Day 10; however, circularity decreased and greater variability between spheroids was observed. Spheroid growth, as measured by LDH release, shown in Figure 4B, was steady but plateaued slightly by Day 21. Based on the diameter, circularity and morphological observations, Day 7 was selected as experimental starting point. Live/dead staining indicated zones of viability and cell death (Figure 4C). Fluorescein fluorescence was more intense at the outer layer of the spheroid and decreased towards the core of the spheroid, where PI fluorescence was predominant.

Cytotoxicity assessments

The measured LDH release for the negative control was 15.9% compared with the 100% of the lysis control. The PCOOH-AuNPs decreased LDH release, non-significantly, by 3.1% and 3.7% after 2 and 24 h exposures, respectively, compared with the negative control. Similarly, uptake inhibitors showed no increase in LDH release after 3 h exposure to inhibitory concentrations thereof (Figure 5).

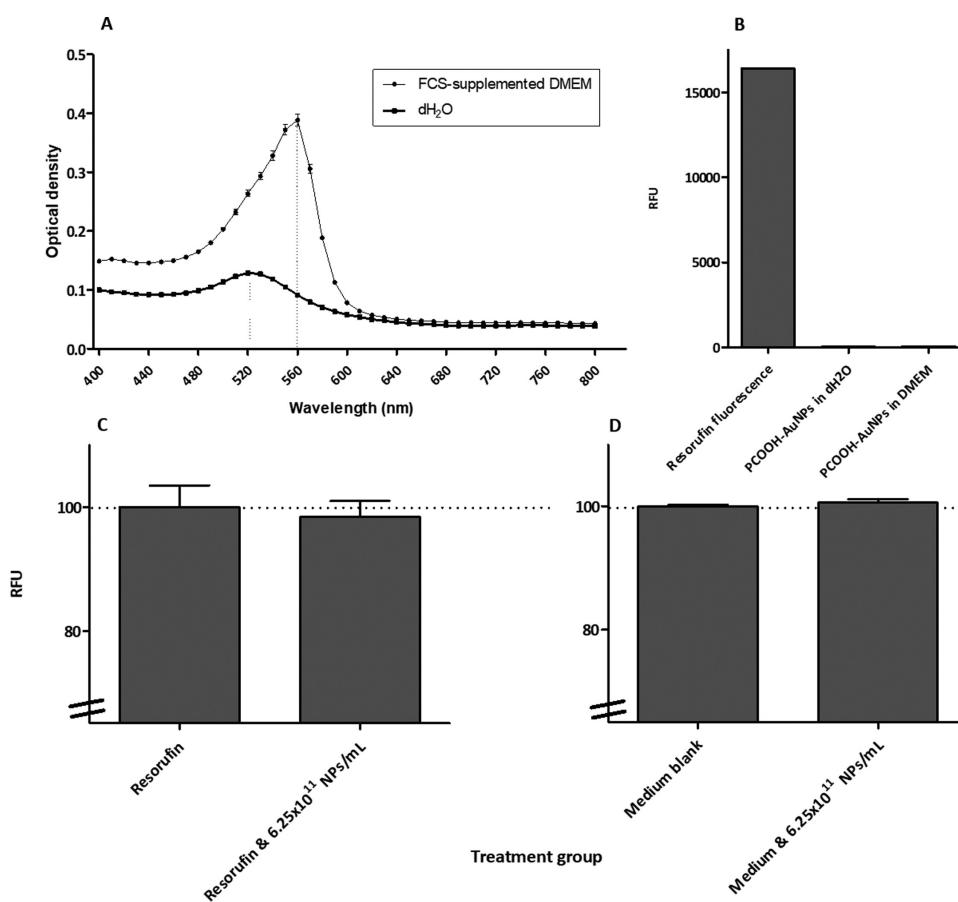


Figure 3 UV-Vis spectroscopy mapping of 6.25×10^{11} NPs/ml PCOOH-AuNPs in FCS-supplemented DMEM and dH_2O (A). Fluorescence intensity of 6.25×10^{11} NPs/ml PCOOH-AuNPs in dH_2O and FCS-supplemented DMEM (B). Resorufin, at experimentally relevant concentration, is indicated for the relative fluorescent scale. The 485/590 nm excitation/emission wavelengths were used for fluorometric maps. NP interference with the LDH assay, in terms of quenching of resorufin fluorescence (C) and non-fluorescent substrate conversion in the absence of cells (D). Measurements were carried out in triplicate, and with three technical repeats. Abbreviations: RFU, relative fluorescence units; ζ , zeta.

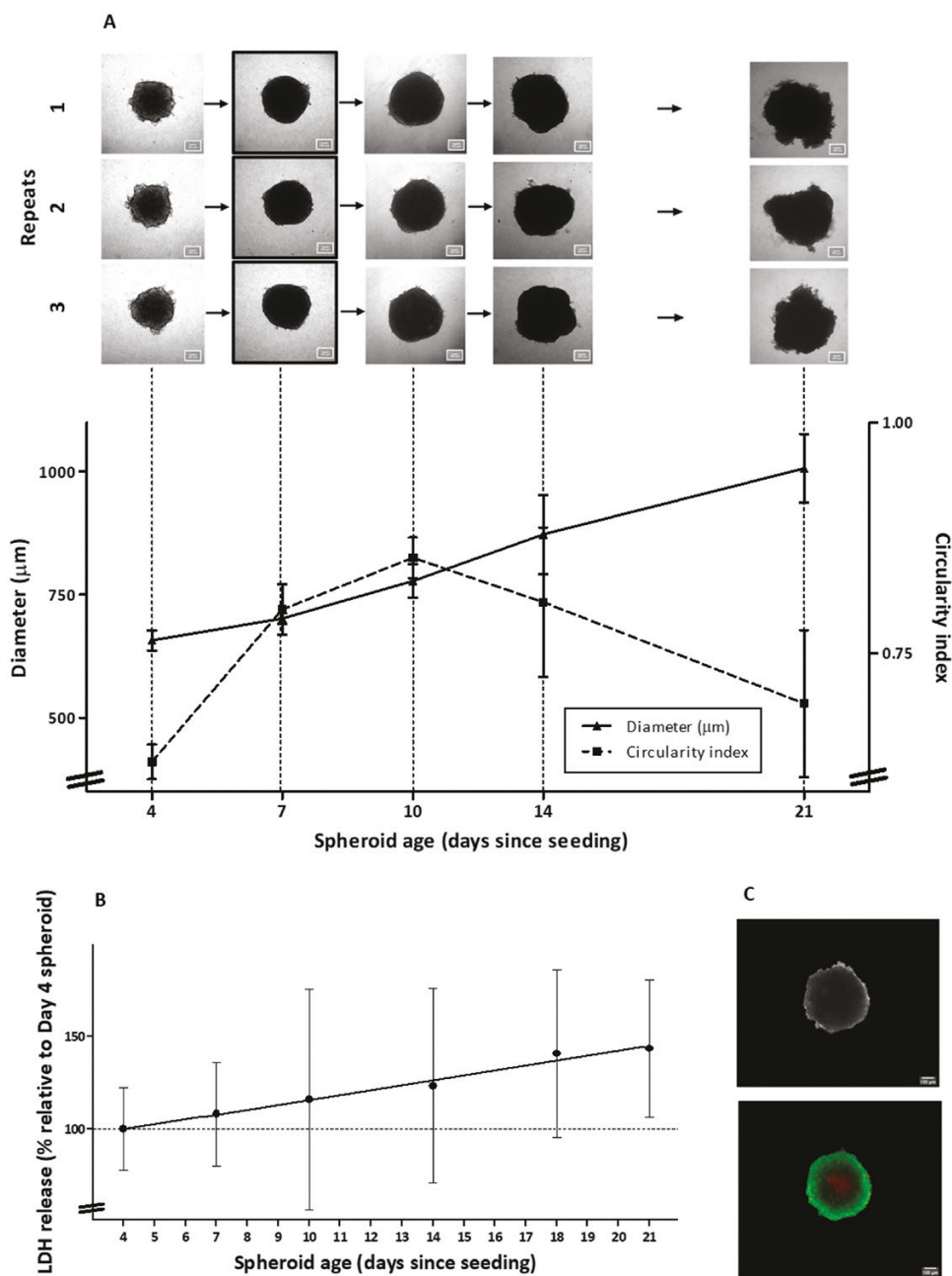


Figure 4 Visual and numerical representation of morphological changes in A549 spheroids over time (A). Outlined are the spheroids at Day 7, when they were considered appropriate for use in all assays in this study. Spheroids shown here are representative images captured over the course of experimentation. Scale bars = 100 μm . Growth of cells within spheroids over time expressed as a percentage relative to Day 4 spheroids (line of best fit) (B). Live/dead staining using FDA/PI, where zones of metabolic activity (green) and areas with compromised cell membranes (red) are shown (phase-contrast image for comparison) (C). Measurements were carried out in a minimum of triplicate, and with three technical repeats.

Spectral angle mapping of internalized PCOOH-AuNPs

A spectral library (Figure 6A) of endocytosed PCOOH-AuNPs was created from an HSI scan of the uninhibited control. Thereafter, background subtraction of the cellular background spectra of a negative control allowed for the generation of a spectral library representative of PCOOH-AuNPs only (Figure 6B). Hyperspectral scans of the spheroids were captured in the form of an HSI (Figure 6C). The PCOOH-AuNP spectral library was mapped onto the scan using the SAM algorithm, and PCOOH-AuNPs counted in a constant area within a region of interest (Figure 6D). The

HSI scans from every treatment class (Figure 6E–L) indicated the accumulation of PCOOH-AuNPs on the periphery of the spheroid, with poor penetration of 4.5 μm (mean value).

NP counts

The 2 and 24 h uninhibited controls displayed 23.5 and 41.6 NPs/area on average, respectively. Comparison between the 2 h and 24 h exposures revealed a non-significant increase of 18.1 NPs/area, while the vehicle control showed a non-significant increase of 2.2 NPs/area. Sodium azide and Dynasore significantly reduced AuNP counts per area by 21.4 NPs/area ($P < 0.0001$) and 15.8 NPs/area ($P < 0.05$),

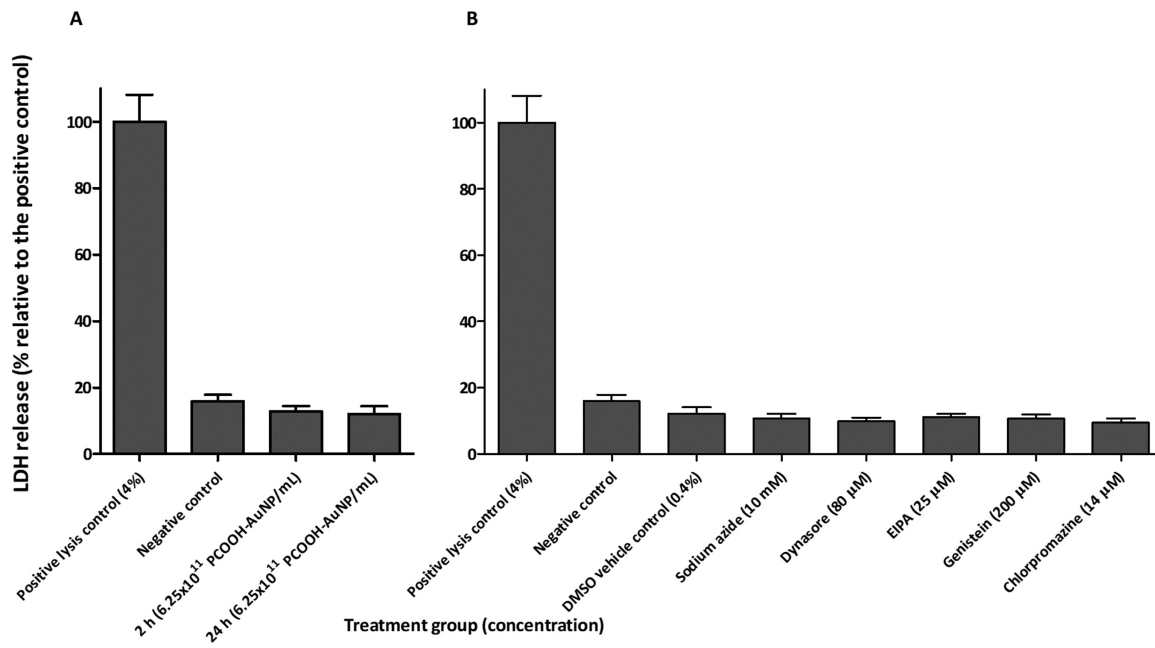


Figure 5 The lack of cytotoxicity after 2 and 24 h exposures to PCOOH-AuNPs (A) and pharmacological inhibitors' after 3 h exposure (B). Measurements were carried out in a minimum of triplicate, and with three technical repeats.

respectively. Non-significant reductions were noted for EIPA (1.5 NPs/area), genistein (0.7 NPs/area) and chlorpromazine (7.9 NPs/area). Using outlier-excluded NP/area counts (Figure 7A), proportions of endocytic mechanisms employed were calculated based on well-documented understandings thereof (Table S1).^[13, 15, 51] The dichotomous inhibitor tree is shown with included uptake proportions in Figure 7B, where an overlap in the employment of CME and CvME was observed.

Discussion

Spheroid formation and growth

Day 7 spheroids were compact, with well-defined edges and high circularity, making them appropriate for experimentation. These features include viability, representative diffusion properties and experimental timeframe.^[27–29] Zones of viability were characteristic of liquid overlay-generated spheroids, where high metabolic activity was noted in the peripheral layers. Spheroids with diameters >1000 μm tend to have larger zones of cell death as a result of poor diffusion of oxygen and nutrients, depriving cells of essential nutrients.^[27, 28] This is similar to what has been noted in in-vivo avascular solid tumours.^[28]

As spheroids grew, they compacted and matured; however, as the liquid overlay model does not continuously renew nutrients or remove metabolic waste, structural integrity was largely diminished after Day 10 with noticeable loss of circularity, compactness and defined edges. Culturing of spheroids for periods exceeding 21 days requires regular nutrient exchange and structural support.^[27] Scaffold-based techniques, bioreactors and co-culturing methods may yield greater longevity.^[27, 52, 53] Compared with 2D cultures, growth is slowed once cells form in 3D, as the ECM reduces growth signalling, which further impacts the longevity.^[29] Live/dead staining allows for the visualization of zonation within spheroids based on viability, providing a more complete picture of growth

patterns. Lower core fluorescein fluorescence corresponds to lower availability of nutrients and O₂, as well as a higher incidence of quiescent cells.^[29, 54] The increased LDH release over the 21 days corroborates spheroid growth and suggests that cells maintain their ability to grow regardless of diminishing structural integrity of the spheroids with age, a caveat of 3D cultures.

Cytotoxicity studies

Assessing cytotoxicity in this study had two purposes: to characterize the effects of the selected PCOOH-AuNPs on the spheroids and to confirm the necessary lack of cytotoxicity in the uptake inhibitors at their inhibitory concentrations. This is a necessary preliminary assessment, as a loss of cell viability due to exposure would confound the uptake investigation. Literature supports the non-toxic nature of the uptake inhibitors in the ranges which reduce uptake pathways' functioning.^[36] Neither the inhibitors nor the PCOOH-AuNPs showed cytotoxicity compared with the negative control. For the purposes and scope of this study, only a single concentration of PCOOH-AuNPs was assessed. A lack of short-term cytotoxicity of similar AuNPs has been reported in the BEAS-2B bronchial epithelial cell line, as well as others, including HepG2 hepatocarcinoma, HEK 293 embryonic kidney, erythrocyte and Cos-1 monkey kidney fibroblast-like cell lines.^[16, 55, 56] This speaks to the inert state of the PCOOH-AuNPs and supports their potential application in drug delivery.^[16]

Uptake and intracellular trafficking of PCOOH-AuNPs into spheroids

The HSI scans allowed for the selection of spectral profiles of the PCOOH-AuNPs within the scanned cellular material, using the "Particle Filter" function of the software, to create a spectral library of the PCOOH-AuNPs. However, cellular material itself can generate background signals, which may

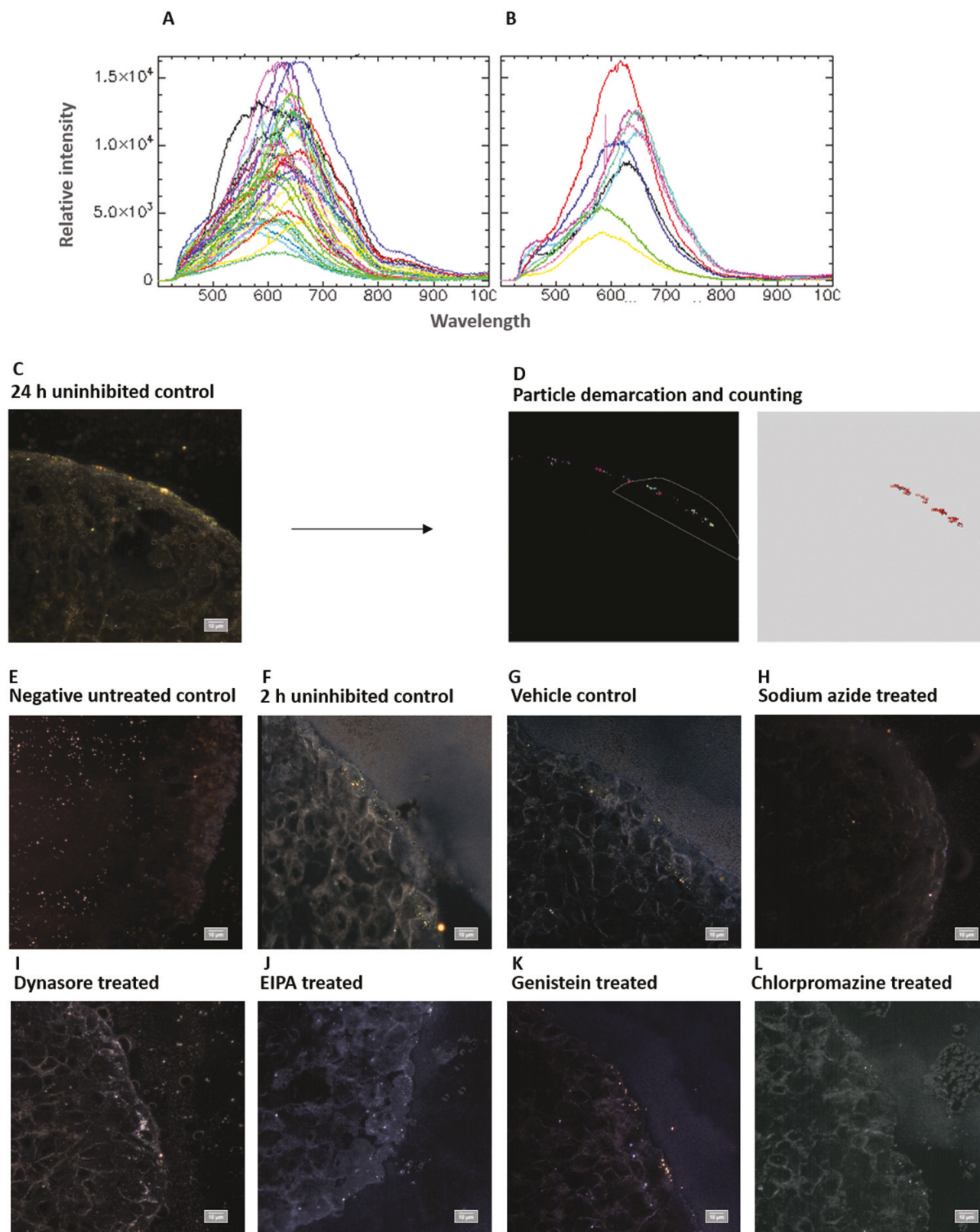


Figure 6 Spectral library plots from a hyperspectral scan of endocytosed PCOOH-AuNPs: (A) all spectra identified as particles included and (B) spectra after subtracting negative control as cellular background. A $\times 60$ hyperspectral scan of 24 h treated, uninhibited control and its SAM image are shown to demonstrate the counting process (C and D). Localization of PCOOH-AuNPs in pharmacological inhibitor-exposed spheroids (E–L); Representative $\times 60$ hyperspectral images captured using CytoViva. Examples of background noise (excluded from analysis) are visible in C, F and K.

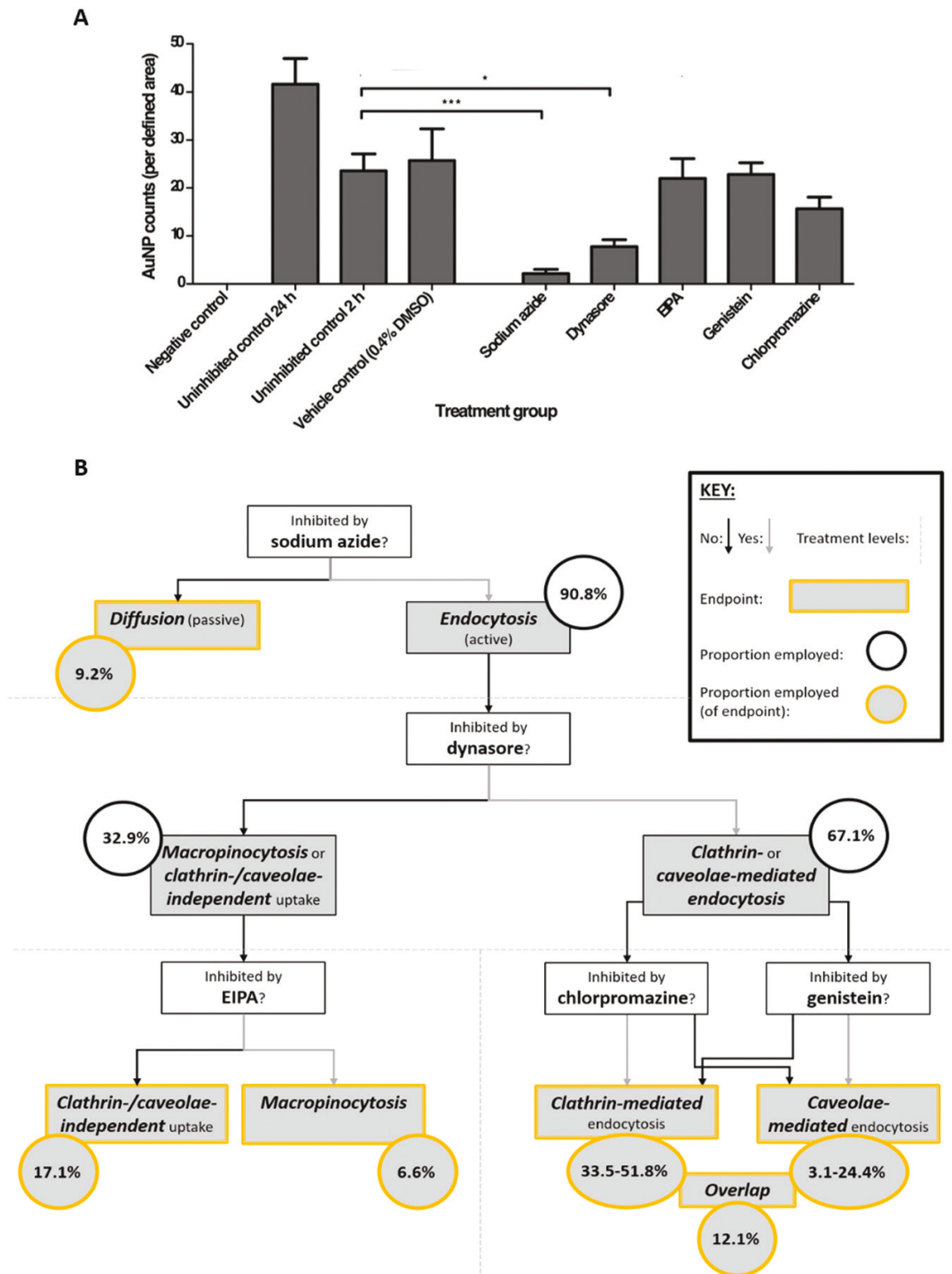


Figure 7 Internalized gold NP counts per defined area, assessed by CytoViva for each treatment group (A). Dichotomous key (as in Figure S1) depicting inhibitor selection and pathway deduction, with added uptake mechanism proportions (rounded to the nearest decimal) (B). Ranges are given for CME and CvME. Measurements were carried out in a minimum of triplicate, and with three technical repeats. * $P < 0.05$; *** $P < 0.0001$.

be incorrectly selected as particles, facilitating possible false PCOOH-AuNP detection during subsequent SAM analyses.^[50] To prevent this, the spectral profiles of cellular material, acquired from the negative control slide, were removed from the spectral library, as successfully described by Roth *et al.*^[50]

This spectral library was then used in SAM analyses to subsequently identify the uptake of PCOOH-AuNPs in spheroid-treated samples.

Low total PCOOH-AuNP uptake, of approximately two PCOOH-AuNPs per cell (24 h), was observed, which contrasts

with previous investigations of 14 nm citrate-capped- and PCOOH-AuNPs in 2D cultures.^[16, 55] In BEAS-2B monolayer cultures, ~100 internalized AuNPs were reported per cell within 4 h.^[36] In monolayer cultures, all cells are uniformly exposed to NPs; however, in the case of spheroids, AuNP penetration efficiency and transcytosis affect uptake due to the 3D architecture of the cellular construct. Comparisons to other studies are few, owing to the unique nature of each synthetic nanomaterial. Additionally, the peri-spheroidal presence of ECM, pH alterations and fluctuating nutrient levels, all affect NP uptake and intracellular destinations.^[57] The AuNPs adsorb proteins, which affects cell–NP interactions and decreases uptake.^[57, 58] Monolayer cultures, which are exposed equally with no multilayer transport required, cannot be compared with spheroids, reaffirming their inability to sufficiently represent or translate to the in-vivo research environment.^[16, 23, 59]

Only a small percentage (9.2%) of PCOOH-AuNPs entered the cells via diffusion, possibly due to partial membrane damage or permeabilized, non-viable cells near the spheroid's surface.^[39] The low observed diffusion may be somewhat due to the negative charge shown by these PCOOH-AuNPs in the culture medium.^[60] Neutral NPs show lower serum protein adsorption, resulting in the retention of their lower hydrodynamic diameter, thus enabling more passive diffusion to take place.^[60–63] Similarly low passive uptake was reported in an NP uptake study using erythrocytes.^[63]

Macropinocytosis, due to its bulk engulfment of the surrounding material, lacks selectivity.^[64] Low employment thereof (6.6%) was observed in this study, which is ascribed to the small size of the NPs. Macropinocytosis is known to be of greater importance for larger particles; however, smaller NPs found in suspension near the cell surface may also be taken up, should size changes allow, for example, during agglomeration.^[58, 65] Trafficking of material taken up by macropinocytosis is largely dependent on the internalized substance, making this difficult to hypothesize.^[64]

Clathrin- and caveolae-independent endocytosis, while poorly characterized,^[13] collectively accounted for 17.1% of uptake. Particles taken up in this way seem to assimilate into other trafficking pathways, making them relatively untargeted subcellularly.^[15] These flotillin-, RhoA-, Cdc-42-, Arf1- and Arf6-mediated pathways are able to fuse with endosomes, thus making degradation possible in the late endosome or lysosome, possibly causing LMP.^[51] A known candidate for clathrin- and caveolae-independent endocytosis is folate.^[58] Studies have found that folate and folate-bound molecules or particles, bound to the folate receptor, are engulfed conservatively and trafficked non-degradatively into the cytoplasm or endosomes.^[58, 66, 67]

In this study, CME was responsible for between 33.5% and 54.8% of PCOOH-AuNP uptake. The pathway directs internalized cargo to endosomes, degradative lysosomes or the plasma membrane.^[58, 60] A lysosomal endpoint is less desirable, because once within a lysosome, particles may be trapped and prevented from exerting action, unless conjugated to a drug activated by enzymes or low pH.^[43, 58] In some cases, lysosomal trafficking may be desired to facilitate LMP, which can lead to mitochondrial membrane damage and autophagy.^[68, 69] Therefore, LMP induction has become a common target for NP-mediated cell killing, though may only take place over longer periods of NP exposure.^[68, 69]

When considering NPs as drug carriers, once within lysosomes, molecules of interest may be degraded before activity is exerted.^[60] This is problematic if the desired effect is not mediated by the NPs themselves, which would make CME less desirable during drug delivery. The process of CME can take place in a receptor-independent manner, via non-specific electrostatic and hydrophobic interactions, rendering it widely applicable.^[58] The fate of an endocytosed substrate is often dependent on cargo-specific interactions with intracellular trafficking machinery after internalizing.^[64, 65] Furthermore, the cationic charge of the PCOOH-AuNPs in this study suggests that they are more thoroughly endocytosed than anionic nanomaterials.^[70] Partiality towards CME, as well as increased plasma membrane–NP interaction, escalates not only the extent but also the rate thereof.^[60, 71] Neutral or negatively charged AuNPs have an 8- and 10-fold decrease in uptake, respectively, into the lung tissue compared with AuNPs carrying a positive charge.^[72] Cell line differences also play a role in pathway selection.^[16] Pathways concluding in lysosomal degradation are not favourable for AuNPs. The intracellular degradation of AuNPs begins with oxidase-mediated ROS induction within the lysosome. The AuNPs remain within cells as nanoleaves, which follow a similar degradation pathway to ionic gold.^[73] Smaller (4 nm) AuNPs are reported to degrade faster than larger AuNPs of the same type.^[73]

The CvME pathway, accounting for between 3.1% and 24.4% of NP uptake into spheroids, trafficks internalized particles to caveosomes and/or endosomes at neutral pH, avoiding degradative fate in the lysosome.^[58, 74] Subcellular trafficking is towards the smooth endoplasmic reticulum (ER) and Golgi complex.^[74] This is the most desirable pathway when considering drug delivery or therapeutics, as the taken-up substance either remains in the intracellular environment (cytosolically or within endosomes) or is transported to deeper cell or tissue layers via transcytosis.^[8, 58, 75] Particles may be targeted towards CvME through functionalizations for specifically activating signalling pathways through phosphorylation.^[60, 75, 76] As such, CvME is largely dependent on its endocytic cargo for the direction of trafficking.^[74]

Pathway overlap

A mechanism employment percentage overlap of 12.1% exists between CME and CvME, which may be due to uptake mechanism efficiency and/or alternative endocytic pathway employment following inhibition. Endocytic rates could play a role in the observed overlap, by allowing uptake to occur more rapidly via one endocytic pathway than another.^[77] Because of the relatively short incubation time employed in this study, the rate at which endocytosis occurred may play a confounding role, as seen in investigations by Rejman *et al.*^[77] It was observed that during the first 30 min of uptake, CME occurred at more than double the rate of CvME, while the extent and rate of both mechanisms became nearly equal after 3 h.^[77] Similarly, cationic NPs are rapidly endocytosed via CME.^[71, 72] Thus, when considering the above results and an NP exposure time of 2 h, employment of CME may have been inflated.

The observed overlap in uptake mechanisms may also imply that a functionality overlap exists between CME and CvME.^[15] Overlapping functionality is plausible given the general rapidly adaptative nature of cancerous cells.^[78, 79] Thus, secondary activation may be worth investigation.

Endocytic pathways and endosomal trafficking are extremely dynamic pathways, as their responses to stimuli differ based on the needs of cells.^[80, 81] Inhibition studies have shown that multiple pathways can be employed by a single cell line, for endocytosis of the same NPs.^[81] A study by Medina-Kauwe corroborates the above, further noting that altered endocytic mechanisms may have worthwhile drug delivery implications.^[82] Directing the uptake and intracellular trafficking of potential drugs presents the possibility of delivering active ingredients to specific intracellular compartments.^[82] This has been achieved by several pathogens, such as the simian virus 40, which uses CvME by binding two CvME-specific receptors, thereby avoiding degradation.^[82–87]

Gold NP penetration and intercellular trafficking

The PCOOH-AuNPs' penetration into the cores of spheroids was relatively low and was not trafficked more than one cell layer deep. This indicates low levels of transcytosis and diffusion, as well as high intracellular retention of PCOOH-AuNPs following endocytosis. Regarding NP size, Perrault *et al.* report that smaller AuNPs (sizes tested: 20–100 nm) tend to show better penetration into vasculature than larger ones.^[60, 88] However, larger NPs (40–100 nm) showed no statistically significant difference between each other, and it was observed that the 20 nm NPs were able to move through interstitial space.^[88] Movement through interstitial space was not emulated in this study's spheroid model; this may be ascribed to the relative simplicity and lack of varying cell types.^[27, 89] Penetration of particles through a spheroid is a function of the employed uptake mechanism. As such, CvME is more likely to facilitate transcytosis.^[58] Therefore, the finding that it is not primarily employed in this study is corroborated by low penetration and transcytosis.^[58] Tailoring NPs to trigger CvME has the potential to increase penetration.^[75] An exemplary application of this knowledge is described by Gradishar.^[76] Briefly, albumin-bound drugs preferentially target CvME, preventing subsequent breakdown and increasing efficacy. Tumour (spheroid) permeability and compaction also play a key role in NP penetration.^[60, 90] In general, poorly permeable tumours were reported as largely unaffected by therapy with a drug and nanocarrier, whereas more permeable tumours indicated increased susceptibility to treatment.^[90] This highlights the importance of consistency and reproducibility in a spheroid model.^[90]

Conclusions

A model was successfully developed for the investigation of PCOOH-AuNP uptake into 3D A549 alveolar carcinoma spheroids using a label-free approach. Spheroids were grown to an appropriate and reproducible size and density within 7 days and, as such, allowed for a platform to be developed for various in-vivo-representative analyses. The PCOOH-AuNPs investigated were not cytotoxic at 6.25×10^{11} NPs/ml to A549 alveolar carcinoma cell spheroids.

HSI and SAM of internalized PCOOH-AuNPs revealed CME to be the primary uptake mechanism employed for these NPs. This is undesirable, given its degradative subcellular destination, but there are advantages to CME, such as its efficiency, lack of receptor specificity and potential for LMP induction. Alternatively, CvME, responsible for the second-highest amount of endocytosis, would be more desirable for

NPs designated for drug delivery and applications thereof. Although these PCOOH-AuNPs did not permeate deeply into the spheroid, evidence of their ability to do so exists and can inform future design of improved, more efficacious AuNPs. NPs of various functionalization are to be tested in the spheroidal model to further elucidate their uptake mechanisms.

Supplementary Material

Supplementary data are available at *Journal of Pharmacy and Pharmacology* online.

Acknowledgement

The authors thank Millicent Magogoty of the National Institute for Occupational Health, National Health Laboratory Service, Johannesburg, South Africa, for assistance with measurements.

Author Contributions

S.-F.F. performed all experimentation and write-up, contributed to conceptualization of the project and analysed all data. M.P. provided assistance throughout and was instrumental in developing the spheroid model used in this research. V.S. provided scientific insight and edited the article. M.G. provided access to crucial equipment, funding and edited the article. M.V. provided guidance on the CytoViva experimentation and edited the article. W.C. conceptualized the work contained herein, edited written elements, provided scientific insight and assisted with the assessment of data analysis.

Funding

This work was supported by the National Research Foundation (NRF), as part of Brazil, Russia, India, China, South Africa (BRICS) Multilateral Joint Science and Technology Research Collaboration Programme [grant number 116017].

Conflicts of Interest

The authors declare that no conflict of interest exists in the context of this study.

Consent for Publication

It is hereby confirmed that all authors are aware of the contents of this manuscript and provide consent for its publication.

Data Availability

Data are available upon request.

References

- Lazzari G, Couvreur P, Mura S. Multicellular tumor spheroids: a relevant 3D model for the *in vitro* preclinical investigation of polymer nanomedicines. *Polym Chem* 2017; 8: 4947–69. <https://doi.org/10.1039/C7PY00559H>
- Dykman L, Khlebtsov N. Gold nanoparticles in biomedical applications: recent advances and perspectives. *Chem Soc Rev* 2012; 41: 2256–82. <https://doi.org/10.1039/c1cs15166e>

3. Ahn S, Lee IH, Kang S et al. Gold nanoparticles displaying tumor-associated self-antigens as a potential vaccine for cancer immunotherapy. *Adv Healthc Mater* 2014; 3: 1194–9. <https://doi.org/10.1002/adhm.201300597>
4. Hainfeldt JF, Dilmanian FA, Slatkin DN et al. Radiotherapy enhancement with gold nanoparticles. *J Pharm Pharmacol* 2008; 60: 977–85. <https://doi.org/10.1211/jpp.60.8.0005>
5. Arvizo RR, Rana S, Miranda OR et al. Mechanism of anti-angiogenic property of gold nanoparticles: role of nanoparticle size and surface charge. *Nanomedicine* 2011; 7: 580–7. <https://doi.org/10.1016/j.nano.2011.01.011>
6. Marchesan S, Prato M. Nanomaterials for (Nano)medicine. *ACS Med Chem Lett* 2013; 4: 147–9. <https://doi.org/10.1021/ml3003742>
7. Sztandera K, Gorzkiewicz M, Klajnert-Maculewicz B. Gold nanoparticles in cancer treatment. *Mol Pharm* 2019; 16: 1–23. <https://doi.org/10.1021/acs.molpharmaceut.8b00810>
8. Gulumian M, Andraos C. In search of a converging cellular mechanism in nanotoxicology and nanomedicine in the treatment of cancer. *Toxicol Pathol* 2018; 46: 4–13. <https://doi.org/10.1177/0192623317735776>
9. Rivera HL, Jara F, Cunningham V. *Modelling and characterization of photothermal effects assisted with gold nanorods in ex-vivo samples and in a murine model*. Proc SPIE 7901, Energy-based Treatment of Tissue and Assessment VI, 79010D (23 February 2011). <https://doi.org/10.1117/12.875706>
10. Jenkins SV, Nedosekin DA, Shaulis BJ et al. Enhanced photothermal treatment efficacy and normal tissue protection via vascular targeted gold nanocages. *Nanotheranostics* 2019; 3: 145–55. <https://doi.org/10.7150/ntno.32395>
11. Nanospectra Biosciences, Inc. *Efficacy Study of AuroLase Therapy in Subjects with Primary and/or Metastatic Lung Tumors*. 2016. <https://clinicaltrials.gov/ct2/show/NCT01679470> (10 November 2020, date last accessed).
12. Bhattacharyya K, Mehta S, Viator J. Optically absorbing nanoparticle mediated cell membrane permeabilization. *Opt Lett* 2012; 37: 4474–6. <https://doi.org/10.1364/OL.37.004474>
13. Conner SD, Schmid SL. Regulated portals of entry into the cell. *Nature* 2003; 422: 37–44. <https://doi.org/10.1038/nature01451>
14. Sutradhar KB, Amin ML. Nanotechnology in cancer drug delivery and selective targeting. *ISRN Nanotech* 2014; 1: 12–3. <https://doi.org/10.1155/2014/939378>
15. Iversen TG, Skotland T, Sandvig K. Endocytosis and intracellular transport of nanoparticles: present knowledge and need for future studies. *Nano Today* 2011; 6: 176–85. <https://doi.org/10.1016/j.nantod.2011.02.003>
16. Vetten M, Gulumian M. Differences in uptake of 14 nm PEG-liganded gold nanoparticles into BEAS-2B cells is dependent on their functional groups. *Toxicol Appl Pharmacol* 2019; 363: 131–41. <https://doi.org/10.1016/j.taap.2018.11.014>
17. Vácha R, Martínez-Veracoechea FJ, Frenkel D. Receptor-mediated endocytosis of nanoparticles of various shapes. *Nano Lett* 2011; 11: 5391–5. <https://doi.org/10.1021/nl2030213>
18. Oh N, Park JH. Endocytosis and exocytosis of nanoparticles in mammalian cells. *Int J Nanomed* 2014; 9: 51–63. <https://doi.org/10.2147/IJN.S26592>
19. Gary-Bobo M, Vaillant O, Maynadier M et al. Targeting multiplicity: the key factor for anti-cancer nanoparticles. *Curr Med Chem* 2013; 20: 1946–55. <https://doi.org/10.2174/0929867311320150002>
20. Yamada KM, Cukierman E. Modeling tissue morphogenesis and cancer in 3D. *Cell* 2007; 130: 601–10. <https://doi.org/10.1016/j.cell.2007.08.006>
21. Ekert JE, Johnson K, Strake B et al. Three-dimensional lung tumor microenvironment modulates therapeutic compound responsiveness *in vitro*—implication for drug development. *PLoS One* 2014; 9: e92248. <https://doi.org/10.1371/journal.pone.0092248>
22. Alemany-Ribes M, Semino CE. Bioengineering 3D environments for cancer models. *Adv Drug Deliv Rev* 2014; 79–80: 40–9. <https://doi.org/10.1016/j.addr.2014.06.004>
23. Pampaloni F, Reynaud EG, Stelzer EH. The third dimension bridges the gap between cell culture and live tissue. *Nat Rev Mol Cell Biol* 2007; 8: 839–45. <https://doi.org/10.1038/nrm2236>
24. Kimlin LC, Casagrande G, Virador VM. *In vitro* three-dimensional (3D) models in cancer research: an update. *Mol Carcinog* 2013; 52: 167–82. <https://doi.org/10.1002/mc.21844>
25. Lee GY, Kenny PA, Lee EH et al. Three-dimensional culture models of normal and malignant breast epithelial cells. *Nat Methods* 2007; 4: 359–65. <https://doi.org/10.1038/nmeth1015>
26. Ghajar CM, Bissell MJ. Tumor engineering: the other face of tissue engineering. *Tissue Eng Part A* 2010; 16: 2153–6. <https://doi.org/10.1089/ten.TEA.2010.0135>
27. Haycock JW. 3D cell culture: a review of current approaches and techniques. *Methods Mol Biol* 2011; 695: 1–15. https://doi.org/10.1007/978-1-60761-984-0_1
28. Cui X, Hartanto Y, Zhang H. Advances in multicellular spheroids formation. *J R Soc Interface* 2017; 14: 20160877. <https://doi.org/10.1098/rsif.2016.0877>
29. Zanoni M, Piccinini F, Arienti C et al. 3D tumor spheroid models for *in vitro* therapeutic screening: a systematic approach to enhance the biological relevance of data obtained. *Sci Rep* 2016; 6: 19103. <https://doi.org/10.1038/srep19103>
30. Theocharis AD, Skandalis SS, Gialeli C et al. Extracellular matrix structure. *Adv Drug Deliv Rev* 2016; 97: 4–27. <https://doi.org/10.1016/j.addr.2015.11.001>
31. da Rocha EL, Porto LM, Rambo CR. Nanotechnology meets 3D *in vitro* models: tissue engineered tumors and cancer therapies. *Mater Sci Eng C Mater Biol Appl* 2014; 34: 270–9. <https://doi.org/10.1016/j.msec.2013.09.019>
32. Bonnans C, Chou J, Werb Z. Remodelling the extracellular matrix in development and disease. *Nat Rev Mol Cell Biol* 2014; 15: 786–801. <https://doi.org/10.1038/nrm3904>
33. Zhang XD, Wu HY, Wu D et al. Toxicologic effects of gold nanoparticles *in vivo* by different administration routes. *Int J Nanomed* 2010; 5: 771–81. <https://doi.org/10.2147/IJN.S8428>
34. Mansour HM, Rhee YS, Wu X. Nanomedicine in pulmonary delivery. *Int J Nanomedicine* 2009; 4: 299–319. <https://doi.org/10.2147/ijn.s4937>
35. De Jong WH, Borm PJ. Drug delivery and nanoparticles: applications and hazards. *Int J Nanomed* 2008; 3: 133–49. <https://doi.org/10.2147/ijn.s596>
36. Vetten MA, Tlotleng N, Tanner Rascher D et al. Label-free *in vitro* toxicity and uptake assessment of citrate stabilised gold nanoparticles in three cell lines. *Part Fibre Toxicol* 2013; 10: 50. <https://doi.org/10.1186/1743-8977-10-50>
37. Senavirathna LK, Fernando R, Maples D et al. Tumor spheroids as an *in vitro* model for determining the therapeutic response to proton beam radiotherapy and thermally sensitive nanocarriers. *Theranostics* 2013; 3: 687–91. <https://doi.org/10.7150/thno.6381>
38. Jones KH, Senft JA. An improved method to determine cell viability by simultaneous staining with fluorescein diacetate-propidium iodide. *J Histochem Cytochem* 1985; 33: 77–9. <https://doi.org/10.1177/33.1.2578146>
39. Boyd V, Cholewa OM, Papas KK. Limitations in the use of fluorescein diacetate/propidium iodide (FDA/PI) and cell permeable nucleic acid stains for viability measurements of isolated Islets of Langerhans. *Curr Trends Biotechnol Pharm* 2008; 2: 66–84. PMID: PMC2931281.
40. Chen W, Wong C, Vosburgh E et al. High-throughput image analysis of tumor spheroids: a user-friendly software application to measure the size of spheroids automatically and accurately. *J Vis Exp* 2014; 8: E51639. <https://doi.org/10.3791/51639>
41. Kramer DN, Guibault GG. A substrate for the fluorometric determination of lipase activity. *Anal Chem* 1963; 35: 588–9. <https://doi.org/10.1021/ac60197a027>
42. Riss T, Moravec R. Introducing the CytoTox-ONE homogeneous membrane integrity assay. *Cell Notes* 2002; 4: 6–9.

43. Kou L, Sun J, Zhai Y et al. The endocytosis and intracellular fate of nanomedicines: implication for rational design. *Asian J Pharm* 2013; 8: 1–10. <https://doi.org/10.1016/j.ajps.2013.07.001>
44. Zhu H, Zhou B, Chan L et al. Transferrin-functionalized nanographene oxide for delivery of platinum complexes to enhance cancer-cell selectivity and apoptosis-inducing efficacy. *Int J Nanomed* 2017; 12: 5023–38. <https://doi.org/10.2147/IJN.S139207>
45. Macia E, Ehrlich M, Massol R et al. Dynasore, a cell-permeable inhibitor of dynamin. *Dev Cell* 2006; 10: 839–50. <https://doi.org/10.1016/j.devcel.2006.04.002>
46. Han SC, Guo HC, Sun SQ et al. Productive entry of foot-and-mouth disease virus via macropinocytosis independent of phosphatidylinositol 3-kinase. *Sci Rep* 2016; 6: 19294. <https://doi.org/10.1038/srep19294>
47. Ivanov AI. Pharmacological inhibition of endocytic pathways: is it specific enough to be useful? *Methods Mol Biol* 2008; 440: 15–33. https://doi.org/10.1007/978-1-59745-178-9_2
48. Commisso C, Flinn RJ, Bar-Sagi D. Determining the macropinocytic index of cells through a quantitative image-based assay. *Nat Protoc* 2014; 9: 182–92. <https://doi.org/10.1038/nprot.2014.004>
49. Vercauteren D, Vandenbroucke RE, Jones AT et al. The use of inhibitors to study endocytic pathways of gene carriers: optimization and pitfalls. *Mol Ther* 2010; 18: 561–9. <https://doi.org/10.1038/mt.2009.281>
50. Roth GA, Sosa Peña Mdel P, Neu-Baker NM et al. Identification of metal oxide nanoparticles in histological samples by enhanced darkfield microscopy and hyperspectral mapping. *J Vis Exp* 2015; 106: e53317. <https://doi.org/10.3791/53317>
51. Manzanares D, Ceña V. Endocytosis: the nanoparticle and submicron nanocompounds gateway into the cell. *Pharmaceutics* 2020; 12: 371–93. <https://doi.org/10.3390/pharmaceutics12040371>
52. Lee J, Cuddihy MJ, Kotov NA. Three-dimensional cell culture matrices: state of the art. *Tissue Eng Part B Rev* 2008; 14: 61–86. <https://doi.org/10.1089/teb.2007.0150>
53. Sethi P, Jyoti A, Swindell EP et al. 3D tumor tissue analogs and their orthotopic implants for understanding tumor-targeting of microenvironment-responsive nanosized chemotherapy and radiation. *Nanomedicine* 2015; 11: 2013–23. <https://doi.org/10.1016/j.nano.2015.07.013>
54. England CG, Gobin AM, Frieboes HB. Evaluation of uptake and distribution of gold nanoparticles in solid tumors. *Eur Phys J Plus* 2015; 130: 231–58. <https://doi.org/10.1140/epjp/i2015-15231-1>
55. Tlotleng N, Vetten MA, Keter FK et al. Cytotoxicity, intracellular localization and exocytosis of citrate capped and PEG functionalized gold nanoparticles in human hepatocyte and kidney cells. *Cell Biol Toxicol* 2016; 32: 305–21. <https://doi.org/10.1007/s10565-016-9336-y>
56. Goodman CM, McCusker CD, Yilmaz T et al. Toxicity of gold nanoparticles functionalized with cationic and anionic side chains. *Bioconjug Chem* 2004; 15: 897–900. <https://doi.org/10.1021/bc049951i>
57. Shi J, Kantoff PW, Wooster R et al. Cancer nanomedicine: progress, challenges and opportunities. *Nat Rev Cancer* 2017; 17: 20–37. <https://doi.org/10.1038/nrc.2016.108>
58. Behzadi S, Serpooshan V, Tao W et al. Cellular uptake of nanoparticles: journey inside the cell. *Chem Soc Rev* 2017; 46: 4218–44. <https://doi.org/10.1039/c6cs00636a>
59. Johnson JI, Decker S, Zaharevitz D et al. Relationships between drug activity in NCI preclinical *in vitro* and *in vivo* models and early clinical trials. *Br J Cancer* 2001; 84: 1424–31. <https://doi.org/10.1054/bjoc.2001.1796>
60. Zhao Z, Ukidve A, Krishnan V et al. Effect of physicochemical and surface properties on *in vivo* fate of drug nanocarriers. *Adv Drug Deliv Rev* 2019; 143: 3–21. <https://doi.org/10.1016/j.addr.2019.01.002>
61. Bewersdorff T, Vonnemann J, Kanik A et al. The influence of surface charge on serum protein interaction and cellular uptake: studies with dendritic polyglycerols and dendritic polyglycerol-coated gold nanoparticles. *Int J Nanomed* 2017; 12: 2001–19. <https://doi.org/10.2147/IJN.S124295>
62. Cullis PR, Chonn A, Semple SC. Interactions of liposomes and lipid-based carrier systems with blood proteins: relation to clearance behaviour *in vivo*. *Adv Drug Deliv Rev* 1998; 32: 3–17. [https://doi.org/10.1016/s0169-409x\(97\)00128-2](https://doi.org/10.1016/s0169-409x(97)00128-2)
63. Rothen-Rutishauser BM, Schürch S, Haenni B et al. Interaction of fine particles and nanoparticles with red blood cells visualized with advanced microscopic techniques. *Environ Sci Technol* 2006; 40: 4353–9. <https://doi.org/10.1021/es0522635>
64. Kumari S, Mg S, Mayor S. Endocytosis unplugged: multiple ways to enter the cell. *Cell Res* 2010; 20: 256–75. <https://doi.org/10.1038/cr.2010.19>
65. Ding L, Yao C, Yin X et al. Size, shape, and protein corona determine cellular uptake and removal mechanisms of gold nanoparticles. *Small* 2018; 14: e1801451. <https://doi.org/10.1002/smll.201801451>
66. Lu Y, Low PS. Folate-mediated delivery of macromolecular anticancer therapeutic agents. *Adv Drug Deliv Rev* 2002; 54: 675–93. [https://doi.org/10.1016/s0169-409x\(02\)00042-x](https://doi.org/10.1016/s0169-409x(02)00042-x)
67. Kelemen LE. The role of folate receptor alpha in cancer development, progression and treatment: cause, consequence or innocent bystander? *Int J Cancer* 2006; 119: 243–50. <https://doi.org/10.1002/ijc.21712>
68. Wang F, Bexiga MG, Anguissola S et al. Time resolved study of cell death mechanisms induced by amine-modified polystyrene nanoparticles. *Nanoscale* 2013; 5: 10868–76. <https://doi.org/10.1039/c3nr03249c>
69. Sipos A, Kim KJ, Sioutas C et al. Evidence for nanoparticle-induced lysosomal dysfunction in lung adenocarcinoma (A549) cells. *Int J Mol Sci* 2019; 20: 5253–69. <https://doi.org/10.3390/ijms20215253>
70. Niora M, Pedersbæk D, Münter R et al. Head-to-head comparison of the penetration efficiency of lipid-based nanoparticles into tumor spheroids. *ACS Omega* 2020; 5: 21162–71. <https://doi.org/10.1021/acsomega.0c02879>
71. Harush-Frenkel O, Debotton N, Benita S et al. Targeting of nanoparticles to the clathrin-mediated endocytic pathway. *Biochem Biophys Res Commun* 2007; 353: 26–32. <https://doi.org/10.1016/j.bbrc.2006.11.135>
72. Elci SG, Jiang Y, Yan B et al. Surface charge controls the suborgan biodistributions of gold nanoparticles. *ACS Nano* 2016; 10: 5536–42. <https://doi.org/10.1021/acsnano.6b02086>
73. Balfourier A, Luciani N, Wang G et al. Unexpected intracellular biodegradation and recrystallization of gold nanoparticles. *Proc Natl Acad Sci U S A* 2020; 117: 103–13. <https://doi.org/10.1073/pnas.1911734116>
74. Kiss AL. Caveolae and the regulation of endocytosis. *Adv Exp Med Biol* 2012; 729: 14–28. https://doi.org/10.1007/978-1-4614-1222-9_2
75. Pelkmans L, Helenius A. Endocytosis via caveolae. *Traffic* 2002; 3: 311–20. <https://doi.org/10.1034/j.1600-0854.2002.30501.x>
76. Gradishar WJ. Albumin-bound paclitaxel: a next-generation taxane. *Expert Opin Pharmacother* 2006; 7: 1041–53. <https://doi.org/10.1517/14656566.7.8.1041>
77. Rejman J, Bragonzi A, Conese M. Role of clathrin- and caveolae-mediated endocytosis in gene transfer mediated by lipo- and polyplexes. *Mol Ther* 2005; 12: 468–74. <https://doi.org/10.1016/j.ymthe.2005.03.038>
78. Epstein T, Gatenby RA, Brown JS. The Warburg effect as an adaptation of cancer cells to rapid fluctuations in energy demand. *PLoS One* 2017; 12: e0185085. <https://doi.org/10.1371/journal.pone.0185085>
79. Di Nicolantonio F, Mercer SJ, Knight LA et al. Cancer cell adaptation to chemotherapy. *BMC Cancer* 2005; 5: 78. <https://doi.org/10.1186/1471-2407-5-78>
80. Di Fiore PP, von Zastrow M. Endocytosis, signaling, and beyond. *Cold Spring Harb Perspect Biol* 2014; 6: a016865. <https://doi.org/10.1101/cshperspect.a016865>

81. dos Santos T, Varela J, Lynch I et al. Effects of transport inhibitors on the cellular uptake of carboxylated polystyrene nanoparticles in different cell lines. *PLoS One* 2011; 6: e24438. <https://doi.org/10.1371/journal.pone.0024438>
82. Medina-Kauwe LK. "Alternative" endocytic mechanisms exploited by pathogens: new avenues for therapeutic delivery? *Adv Drug Deliv Rev* 2007; 59: 798–809. <https://doi.org/10.1016/j.addr.2007.06.009>
83. Anderson HA, Chen Y, Norkin LC. Bound simian virus 40 translocates to caveolin-enriched membrane domains, and its entry is inhibited by drugs that selectively disrupt caveolae. *Mol Biol Cell* 1996; 7: 1825–34. <https://doi.org/10.1091/mbc.7.11.1825>
84. Pelkmans L, Kartenbeck J, Helenius A. Caveolar endocytosis of simian virus 40 reveals a new two-step vesicular-transport pathway to the ER. *Nat Cell Biol* 2001; 3: 473–83. <https://doi.org/10.1038/35074539>
85. Aguzzi A. Prions and the immune system: a journey through gut, spleen, and nerves. *Adv Immunol* 2003; 81: 123–71. [https://doi.org/10.1016/s0065-2776\(03\)81004-0](https://doi.org/10.1016/s0065-2776(03)81004-0)
86. Haïk S, Faucheux BA, Hauw JJ. Brain targeting through the autonomous nervous system: lessons from prion diseases. *Trends Mol Med* 2004; 10: 107–12. <https://doi.org/10.1016/j.molmed.2004.01.008>
87. Lord JM, Roberts LM. Toxin entry: retrograde transport through the secretory pathway. *J Cell Biol* 1998; 140: 733–6. <https://doi.org/10.1083/jcb.140.4.733>
88. Perrault SD, Walkey C, Jennings T et al. Mediating tumor targeting efficiency of nanoparticles through design. *Nano Lett* 2009; 9: 1909–15. <https://doi.org/10.1021/nl900031y>
89. Costa EC, de Melo-Diogo D, Moreira AF et al. Spheroids formation on non-adhesive surfaces by liquid overlay technique: considerations and practical approaches. *Biotechnol J* 2018; 13. <https://doi.org/10.1002/biot.201700417>
90. Cabral H, Matsumoto Y, Mizuno K et al. Accumulation of sub-100 nm polymeric micelles in poorly permeable tumours depends on size. *Nat Nanotechnol* 2011; 6: 815–23. <https://doi.org/10.1038/nnano.2011.166>